

# Rigorous theoretical study of finite-size two-dimensional photonic crystals doped by microcavities

G. Tayeb and D. Maystre

*Laboratoire d'Optique Electromagnétique, Unité Propre d'Enseignement Supérieur Associée au Centre National de la Recherche Scientifique, No. 6079, Faculté des Sciences et Techniques de St Jérôme, Case 262, 13397 Marseille Cedex 20, France*

Received December 3, 1996; revised manuscript received May 20, 1997; accepted May 27, 1997

We use a rigorous method for diffraction by a finite set of parallel cylinders to study the influence of defects in a photonic crystal. The method allows us to give an accurate description of all the characteristics of the electromagnetic field (near-field map, scattered field, and energy flow). The localized resonant modes can also be computed. We show some of their symmetry properties and the influence of coupling between two neighboring defects. Finally, an example is given, which shows that a slight local change in the crystal period can be used for the realization of devices that radiate energy in a very narrow angular range. © 1997 Optical Society of America [S0740-3232(97)01911-X]

## 1. INTRODUCTION

Basically, photonic crystals are derived from periodic structures. Because of the periodicity, they exhibit photonic band gaps, which means that electromagnetic fields cannot propagate in such structures in a given range of frequencies and directions. It is well known that the introduction of defects in the periodic lattice generates localized electromagnetic modes. In this way high-quality optical microcavities can be obtained. Potential applications in many technological areas, such as the development of efficient semiconductor light emitters, filters, substrates for antennas in microwaves, and lossless mirrors, have generated a growing interest in the study of the properties of photonic band-gap materials.

We present a numerical study of two-dimensional photonic structures of finite extension (the photonic crystal is a finite set of parallel rods). For this purpose we use a rigorous theory in which each rod is characterized by its scattering matrix, which links the diffracted field to the incoming one, these fields being represented by Fourier-Bessel expansions. From translation properties of Bessel functions, the scattering problem is reduced to the resolution of a linear system. The method is numerically efficient and can be implemented on a desktop workstation with short computation times. This approach is completely different from the other theories generally used for such devices: for instance, the plane-wave expansion method in which the fields are expanded in a set of harmonic modes and the resulting eigenvalue problem is solved with a variational principle,<sup>1,2</sup> or the transfer-matrix method.<sup>3,4</sup> In these last two methods, problems involving finite-size crystals with defects<sup>4,5</sup> are solved with the supercell approximation, which replaces the non-periodic structure by a periodic one. The preceding methods solve the problem in the frequency domain. A different approach<sup>5</sup> is able to deal with the time domain.

Experimental studies of the influence of defects in two-dimensional photonic structures have also been published (see, for instance, Refs. 6–8).

The theory is briefly described in Section 2, and its most interesting features are pointed out. It is shown how all electromagnetic quantities (near-field map, scattered field, and energy flow) can be rigorously computed and also how the resonant modes of the structure can be obtained. Section 3 illustrates the method for a simple example with one defect (one cylinder is removed). A comparison between the transmission of a finite-size crystal and an infinite one is also given. Sections 4 and 5 concern crystals with two defects, and we pay attention to the coupling between the resonant modes and their symmetry properties. In Section 6 we present a structure in which one part of the crystal has been expanded in one direction. In this way the emission can be strongly concentrated in a very narrow angular range.

## 2. THEORY AND NOTATION

In this study we are concerned with a periodic and finite set of parallel cylinders lying in vacuum and presenting some defects [Fig. 1(a)]. These defects are obtained by removing some cylinders inside the crystal in order to get microcavities.

The first step is to find adequate parameters for the cylinders—index  $\nu$ , radius  $\rho$ , and crystal geometry—in order to get a band gap (i.e., conditions in which no propagation occurs in the crystal for a certain range of wavelengths and for any direction). For that purpose we can consult, for instance, Ref. 2, in which an atlas of band gaps for two-dimensional crystals is given. In the present work, we have used a computer code dealing with gratings and based on an integral method.<sup>9</sup> This code makes use of the periodicity and allows us to investigate

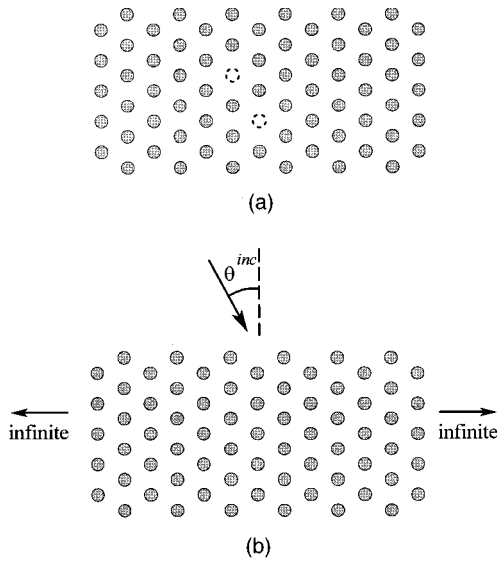


Fig. 1. (a) Finite crystal (11 layers of six or seven cylinders) with two defects, (b) associated periodic crystal dealt by our integral grating code (11 grids that are infinite in the horizontal direction).

with short computation time the properties of photonic crystals such as that presented in Fig. 1(b). On the other hand, this code cannot handle defects, on account of the break of periodicity. Throughout the paper we retain a crystal with a hexagonal symmetry, and the polarization is chosen in such a way that the electric field is parallel to the cylinders (we denote this polarization case by  $E_{\parallel}$ ). In these conditions, with denoting  $d$  the cylinder spacing (distance between the centers of the closest cylinders), a band gap exists for a radius-to-spacing ratio  $\rho/d$  close to 0.15 and for an optical index of the cylinders of  $\nu = 2.9$ .

For the study of finite-size crystals [Fig. 1(a)], we use a rigorous code based on a modal theory.<sup>10</sup> This code has also been used for the study of the localization of light by a set of parallel cylinders.<sup>11</sup> We give below an outline of the main features of this method. The reader interested in more details is directed to Ref. 10.

Let us consider a set of  $N$  parallel cylinders  $\mathcal{C}_j$ ,  $j = 1, \dots, N$  (they can be of arbitrary shape, index, and position), as shown in Fig. 2. The medium outside the cylinders is vacuum. The problem is two dimensional: The cylinders are infinite in the  $z$  direction parallel to the cylinders, and the incident field is also  $z$  invariant. We consider a harmonic problem with wavelength  $\lambda$  and pulsation  $\omega$ , and the fields are represented by their associated complex vectors, with a time dependence in  $\exp(-i\omega t)$ , with  $k = \omega \sqrt{\epsilon_0 \mu_0} = 2\pi/\lambda$ . Since we assume  $E_{\parallel}$  polarization, the problem reduces to a scalar problem in which the unknown is the  $z$  component  $E_z$  of the electromagnetic field. The incident field  $E_z^{\text{inc}}$  is arbitrary. In the numerical examples shown in the following sections, it will be, for instance, a plane wave with a wave vector in the  $x$ - $y$  plane or the field generated by an infinitely thin wire parallel to the  $z$  axis, flown by a filament current and acting as an antenna.

For any cylinder  $\mathcal{C}_j$ , we consider a circle  $\mathcal{D}_j$  with center  $O_j$  in such a way that the cylinder is completely inside  $\mathcal{D}_j$ . Because of the properties of the Helmholtz equation, the

total field at a point  $P$  on  $\mathcal{D}_j$  can be written as a Fourier-Bessel expansion. Denoting by  $r_j(P)$  and  $\theta_j(P)$  the polar coordinates in the local system  $(O_j, x_j, y_j)$ , we can write

$$E_z(P) = \sum_{m=-\infty}^{+\infty} [a_{j,m} J_m(kr_j(P)) + b_{j,m} H_m^{(1)}(kr_j(P))] \exp[im\theta_j(P)]. \quad (1)$$

The two terms in the preceding series can be interpreted in the following way.

The second term satisfies a radiation condition and thus represents the field scattered by the cylinder  $\mathcal{C}_j$ . For each cylinder this scattered field will be characterized by the column matrix  $\mathbf{b}_j$  containing the  $b_{j,m}$  elements.

The first term represents the local incident field on the cylinder  $\mathcal{C}_j$ , generated by the actual incident field  $E_z^{\text{inc}}$  as well as by the fields scattered by all the other cylinders  $\mathcal{C}_k$  with  $k \neq j$ . Denoting by  $\mathbf{a}_j$  the column matrix containing the  $a_{j,m}$  and using translation properties of Bessel functions (Graf's formula<sup>12</sup>), one can obtain<sup>10</sup> for any cylinder  $\mathcal{C}_j$  a linear relationship:

$$\mathbf{a}_j = \mathbf{Q}_j + \sum_{k \neq j} \mathbf{T}_{j,k} \mathbf{b}_k, \quad (2)$$

where  $\mathbf{Q}_j$  is a known column matrix that represents the actual incident field on the cylinder  $\mathcal{C}_j$  and  $\mathbf{T}_{j,k}$  is a known square matrix (its elements simply contain exponentials and Hankel functions). For any cylinder  $\mathcal{C}_j$ , another relationship between  $\mathbf{b}_j$  and  $\mathbf{a}_j$  is provided by the scattering matrix  $\mathbf{S}_j$  of the cylinder. The diffracted field is linked to the local incident field by

$$\mathbf{b}_j = \mathbf{S}_j \mathbf{a}_j. \quad (3)$$

Eliminating  $\mathbf{a}_j$  from Eqs. (2) and (3) and then collecting the equations written for each cylinder lead to a linear system that gives the solution  $\mathbf{b}_j$ :

$$\begin{bmatrix} \mathbf{I} & -\mathbf{S}_1 \mathbf{T}_{1,2} & \cdots & -\mathbf{S}_1 \mathbf{T}_{1,N} \\ -\mathbf{S}_2 \mathbf{T}_{2,1} & \mathbf{I} & \cdots & -\mathbf{S}_2 \mathbf{T}_{2,N} \\ \vdots & \vdots & \ddots & \vdots \\ -\mathbf{S}_N \mathbf{T}_{N,1} & -\mathbf{S}_N \mathbf{T}_{N,2} & \cdots & \mathbf{I} \end{bmatrix} \begin{pmatrix} \mathbf{b}_1 \\ \mathbf{b}_2 \\ \vdots \\ \mathbf{b}_N \end{pmatrix} = \begin{pmatrix} \mathbf{S}_1 \mathbf{Q}_1 \\ \mathbf{S}_2 \mathbf{Q}_2 \\ \vdots \\ \mathbf{S}_N \mathbf{Q}_N \end{pmatrix}, \quad (4)$$

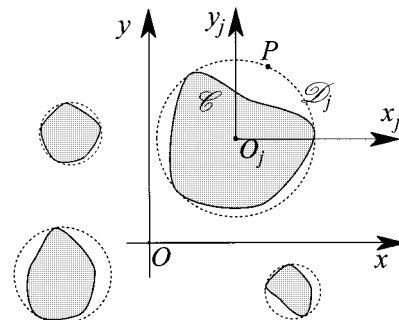


Fig. 2. Scattering by a set of parallel cylinders of arbitrary shape, index, and position.

where  $\mathbf{I}$  denotes the identity matrix. For brevity, this equation will be written as

$$\mathbf{S}^{-1}\mathbf{B} = \mathbf{A} \quad (5)$$

and formally inverted as

$$\mathbf{B} = \mathbf{S}\mathbf{A}. \quad (6)$$

Now let us point out some features of the method.

1. In Eq. (6) column  $\mathbf{A}$  linearly depends on the actual incident field  $E_z^{\text{inc}}$ , and column  $\mathbf{B}$  contains the information on the field diffracted by the entire set of cylinders. In that sense  $\mathbf{S}$  is the scattering matrix of the set of cylinders. From Eq. (4) it appears that  $\mathbf{S}^{-1}$  is simply built as soon as the scattering matrices  $\mathbf{S}_j$  of all cylinders are known. This feature is interesting from a numerical point of view. It means that the individual scattering matrices  $\mathbf{S}_j$  can be constructed independently from the main code dealing with the set of cylinders. In this paper, where the cylinders are circular, the matrices  $\mathbf{S}_j$  are very simple and reduce to diagonal matrices whose elements can be expressed in closed form. But when the cylinders are arbitrarily shaped, we use an external integral code to compute the  $\mathbf{S}_j$ . Another important point is that, when all the cylinders in the set are identical, all the matrices  $\mathbf{S}_j$  are also identical (because they are defined in the local coordinate system centered on each cylinder).

2. Solving system (4) gives the  $b_{j,m}$ . From that knowledge the total electric field  $E_z$  is given outside the circles  $\mathcal{D}_j$  by

$$E_z(P) = E_z^{\text{inc}}(P) + \sum_{j=1}^N \sum_{m=-\infty}^{+\infty} b_{j,m} H_m^{(1)}(kr_j(P)) \exp[im\theta_j(P)]. \quad (7)$$

Taking the gradient of this expression, we get the magnetic-field components. The Poynting vector can finally be deduced from all these expansions. The important point is that the field and the Poynting vector can be obtained in closed form anywhere outside the circles  $\mathcal{D}_j$  from expansions with  $b_{j,m}$  coefficients and involving known functions (exponentials and Bessel). In the case of circular cylinders, circles  $\mathcal{D}_j$  coincide with the surface of the cylinders, and moreover we are able to find similar expansions inside the cylinders. The consequence is that we can plot exact field and Poynting vector maps for any region of space. Of course, the far-field characteristics (intensity at infinity or bistatic differential cross section) are also easily obtainable.

3. For numerical purposes it is clear that the series in Eq. (1) has to be truncated. It can be shown that, because of properties of the Helmholtz equation, the terms of the series are decreasing extremely fast after a given threshold is reached. Assuming that we keep  $M$  terms in the series, columns  $\mathbf{a}_j$  and  $\mathbf{b}_j$  reduce to  $M$  elements, matrices  $\mathbf{S}_j$  have a rank  $M$ , and linear system (4) has a rank  $NM$ . In fact, the value of  $M$  is closely linked with the radius  $\rho$  of the cylinders and the wavelength  $\lambda$ , and a convenient value for  $M$  is given by the empirical rule  $M \approx 40\rho/\lambda$  (taking  $M$  as an odd integer, at least equal to 1). With such a value of  $M$ , the accuracy is better than 1%.

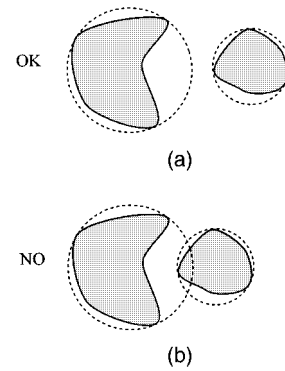


Fig. 3. The circles containing each cylinder must have no intersection.

As an example, typical values used hereafter are  $\rho = 0.6$  and  $\lambda = 9$ , which gives  $M = 3$ . This means that for  $N = 100$  cylinders, we solve a  $300 \times 300$  system. All computations have been performed on a desktop workstation. As a general rule, all the following results have been computed by increasing  $M$  until no difference can be observed on the curves or the maps.

4. The incident field is arbitrary. In the following sections, some examples deal with an incident plane wave with incidence  $\theta^{\text{inc}}$  on the main face of the crystal [as in Fig. 1(b)]. In that case

$$E_z^{\text{inc}}(x, y) = \exp[ik(x \sin \theta^{\text{inc}} - y \cos \theta^{\text{inc}})]. \quad (8)$$

In some other examples, the source is an infinitely thin wire parallel to the  $z$  axis, acting as an antenna. If the position of this antenna in the  $x$ - $y$  plane is  $\mathbf{r}_0$ , the incident field will be taken as

$$E_z^{\text{inc}}(\mathbf{r}) = H_0^{(1)}(k\|\mathbf{r} - \mathbf{r}_0\|). \quad (9)$$

5. Another fundamental feature is to get the resonant modes of the set of cylinders. We define these modes as solutions of Maxwell's equations without any incident field. In this case we have  $E_z^{\text{inc}} = 0$ , and system (5) reduces to

$$\mathbf{S}^{-1}\mathbf{B} = \mathbf{0}. \quad (10)$$

At this step one must keep in mind that the scattering matrix  $\mathbf{S}$  can be considered as a function of the wavelength  $\lambda$ . Equation (10) has solutions only for discrete values  $\lambda_p$  of  $\lambda$ , which are the poles of the  $\mathbf{S}$  matrix:

$$\det[\mathbf{S}^{-1}(\lambda_p)] = 0 \quad (11)$$

or, equivalently,

$$\det[\mathbf{S}(\lambda_p)] = \infty. \quad (12)$$

These complex values  $\lambda_p$  are obtained numerically by searching for the roots of  $\det[\mathbf{S}^{-1}(\lambda)]$ . For each of these wavelengths  $\lambda_p$ , we can further get the resonant mode [the  $\mathbf{B}$  column associated with the mode is nothing other than the eigenvector of  $\mathbf{S}^{-1}(\lambda_p)$  associated with the eigenvalue 0].

6. Last, we must point out one limitation of the method. The Fourier-Bessel expansion in Eq. (1) is valid only if the circle  $\mathcal{D}_j$  lies in a homogeneous medium. This means that the circle that contains one cylinder cannot intersect the boundary of another cylinder. In other

words, the circles  $\mathcal{D}_j$  must have no intersection (Fig. 3). Of course, this is always so when the cylinders are circular. In fact, for noncircular cylinders, the problem is much more subtle, and the method should also work in some cases in which the circles intersect. The problem is similar to the problem of validity of the Rayleigh hypothesis in grating theory.<sup>13-15</sup>

### 3. CRYSTAL WITH ONE DEFECT

In this section we illustrate the capabilities of our computer code in the case of a photonic crystal with one defect. Figure 4 shows the geometry of the crystal. It is composed of a set of dielectric circular cylinders with radius  $\rho = 0.6$ , spacing  $d = 4$ , and optical index  $\nu = 2.9$ .

Figure 5(a) gives the transmission of this crystal versus the wavelength. To compute this transmission, the incident field is a plane wave with normal incidence [coming from the top of Fig. 4, i.e.,  $\theta^{\text{inc}} = 0^\circ$  in Eq. (8)]. We compute the flux of the Poynting vector  $\Phi^{\text{trans}}$  for the total field on a segment lying below the crystal (see Fig. 4). We also compute the flux of the Poynting vector  $\Phi^{\text{inc}}$  for the incident plane wave on the same segment. We define the transmission as  $T = \Phi^{\text{trans}}/\Phi^{\text{inc}}$ . Of course, the segment must be short enough, since it must not collect the power flowing around the crystal (see Fig. 4). Figure 5(a) also gives the transmission for the same crystal as that of Fig. 4, but with no defect (dashed curve; the central cylinder has not been removed). The gap lies between wavelengths 7.3 and 10.8. When the central cylinder is removed (solid curve), a sharp transmission peak appears at wavelength  $\lambda \approx 9.06$ . This is due to the fact that, at this wavelength, a resonance occurs in the microcavity made by the defect, this microcavity playing the role of a relay for photons.

Figure 5(b) compares the transmission of a finite crystal and of a periodic crystal with infinite extension in the horizontal direction [as shown in Fig. 1(b)]. The dashed curve has the same meaning as that in Fig. 5(a). The solid curve has been computed by our code dealing with gratings and based on an integral method<sup>9</sup> for a crystal

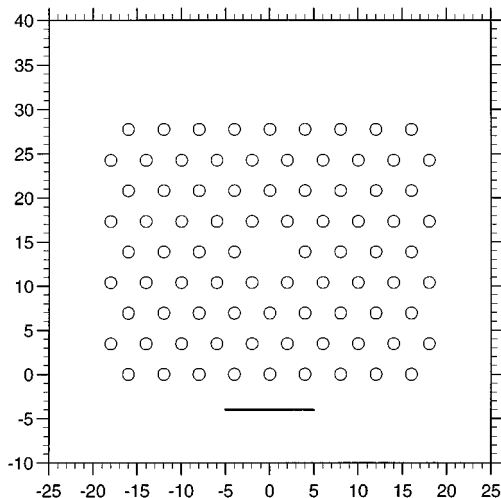


Fig. 4. Crystal with one defect. The segment below the structure is the one used for the computation of the transmission.

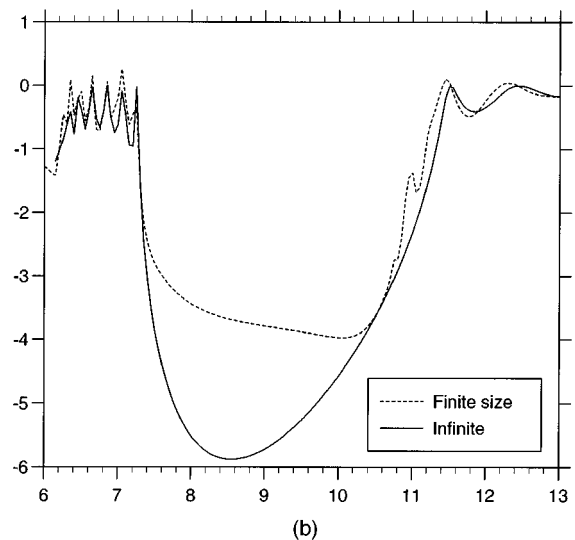
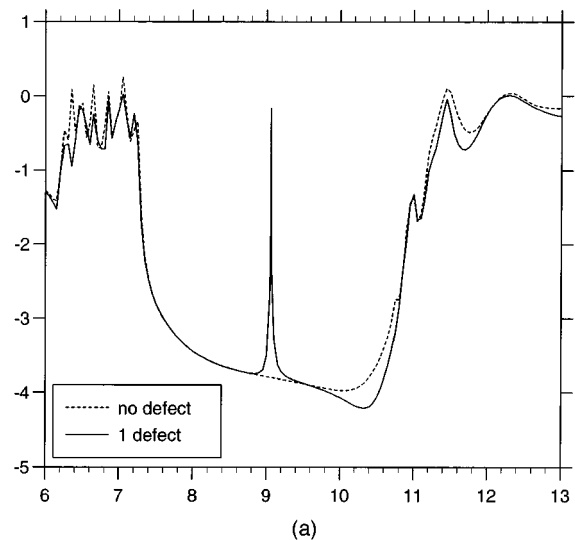


Fig. 5. (a) Decimal logarithm of the transmission  $T$  versus the wavelength for the crystal of Fig. 4 (solid curve) and for the same crystal, but with no defect (dashed curve). (b) Dashed curve: same meaning as that of the dashed curve in (a) (finite crystal of Fig. 4 with no defect); solid curve: curve obtained for a crystal with infinite extension in the horizontal direction. The wavelength sampling pitch is equal to 0.05, with some extra points near the central peak of (a).

with the same parameters (nine grids that are infinite in the horizontal direction). In that case the transmission is simply given by the grating efficiency in the zero transmitted order. A very good agreement between the two curves can be observed. Indeed, the limits of the gap agree quite well, as well as the oscillations of the transmission outside the gap. Some extra oscillations appear on the right-hand limit of the gap with the finite crystal. The difference between the transmissions inside the gap can be easily explained: For the finite crystal, the segment used for the computation of the transmission collects a small part of the energy flowing around the crystal in such a way that the transmission never falls under  $10^{-4}$ . This is not the case for the infinite crystal.

For the crystal with one defect (Fig. 4), the resonance can be studied with more detail by searching the resonant

mode. A numerical research of the poles of the **S** matrix gives the complex resonant wavelength  $\lambda_p = 9.0572 + i0.00092$ . Figure 6 gives the field map for this mode. The small imaginary value of  $\lambda_p$  is related to the fact that the mode has losses: Energy radiates out of the crystal. When the size of the crystal is increased, these losses decrease and consequently the imaginary part of  $\lambda_p$  decreases too. For example, we have considered the same crystal, but now surrounded by two additional rows of cylinders (13 layers of 13 or 14 cylinders instead of nine layers of nine or ten cylinders as in Fig. 4). In this case the resonant wavelength is found to be  $\lambda_p = 9.0572 + i0.000028$ .

Figure 7 shows the Poynting vector map for the crystal illuminated in normal incidence by a plane wave with  $\lambda = \text{Re}(\lambda_p) = 9.0572$ . An arrow has been placed on each point of the grid, giving the direction of the Poynting vector. The size of the arrow is proportional to the modulus of the Poynting vector. This map shows the light travel

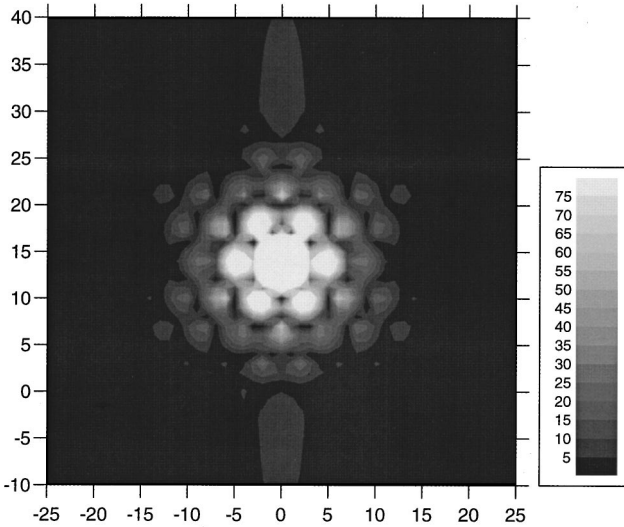


Fig. 6. Modulus of the field associated with the resonant mode for  $\lambda_p = 9.0572 \pm i0.00092$ . The crystal is the one shown in Fig. 4.

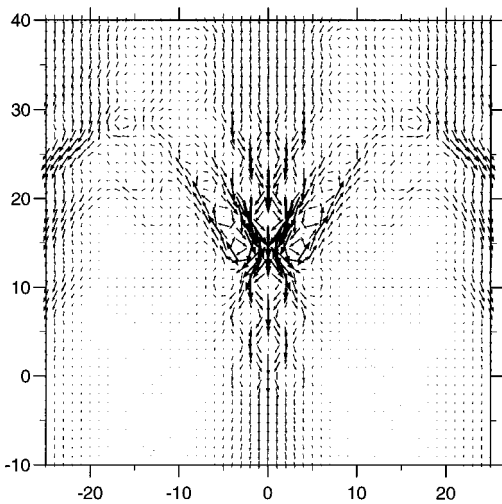


Fig. 7. Poynting vector map for the crystal of Fig. 4, illuminated by a plane wave with  $\lambda = 9.0572$  in normal incidence.

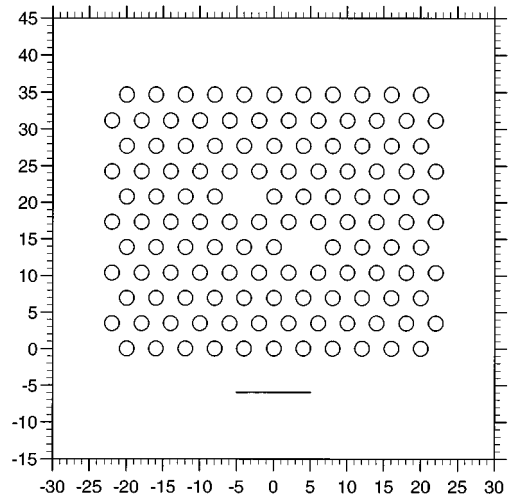


Fig. 8. Crystal with two distant defects. The segment below the structure is the one used for the computation of the transmission.

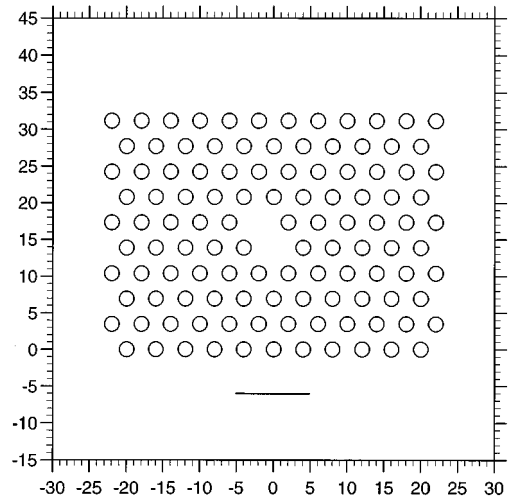


Fig. 9. Crystal with two close defects. The segment below the structure is the one used for the computation of the transmission.

through the crystal and clearly explains the transmission peak of Fig. 5.

#### 4. COUPLING BETWEEN DEFECTS

We now consider a crystal with the same parameters as those in Section 3, but with two defects. Figures 8 and 9 show two crystals with different distances between the defects. Figure 10 gives a comparison of the transmission curves for the different crystals illuminated by a plane wave in normal incidence. In the case of two defects we now get two resonant modes. In Fig. 8 the transmission peaks occur for  $\lambda = 8.985$  and  $\lambda = 9.135$ , whereas for Fig. 9 they occur for  $\lambda = 8.525$  and  $\lambda = 9.655$ . It can be seen that the usual rule applies: As the coupling between the microcavities is increased, the resonant wavelengths of the modes are more split.

#### 5. INFLUENCE OF SYMMETRIES

We still consider a crystal with the same parameters as those in Sections 3 and 4 and with two defects. We con-

sider two situations (Figs. 11 and 12) in which the same crystal has been rotated with an angle of  $90^\circ$ . Figure 13 shows the transmission of these two crystals illuminated by a plane wave in normal incidence. Only one transmission peak appears for the crystal of Fig. 12. The explanation comes from the observation of the field maps of the resonant modes. Since the modes are characteristic of the structure (they are solutions of Maxwell's equations with no incident field), they are obviously independent of any rotation of the crystal. We have found two modes for the complex wavelengths  $\lambda_{p1} = 8.8335 + i0.0162$  and  $\lambda_{p2} = 9.3210 + i0.0159$ . Figures 14 and 15 show the real part of the complex field for these two modes. The first one (Fig. 14) is symmetrical with respect to the horizontal symmetrical axis of the crystal, whereas the second one (Fig. 15) is antisymmetrical. When the crystal of Fig. 12

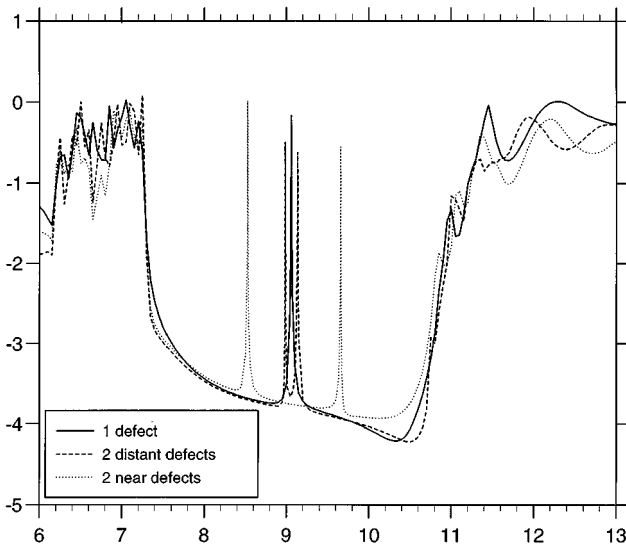


Fig. 10. Decimal logarithm of the transmission  $T$  versus the wavelength for the crystals of Figs. 4 (solid curve), 8 (dashed curve), and 9 (dotted curve). Note that the wavelength sampling pitch is equal to 0.05, with some extra points near the peaks.

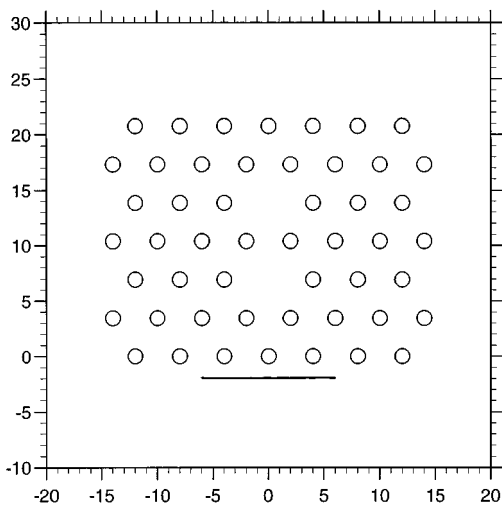


Fig. 11. Crystal with two defects. The segment below the structure is the one used for the computation of the transmission.

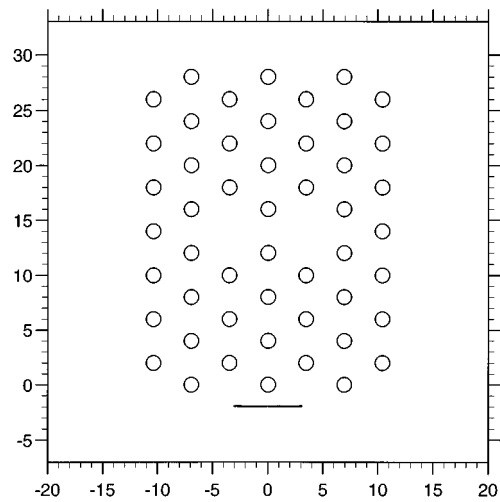


Fig. 12. Same crystal as that of Fig. 11, but rotated  $90^\circ$ . The segment below the structure is the one used for the computation of the transmission.

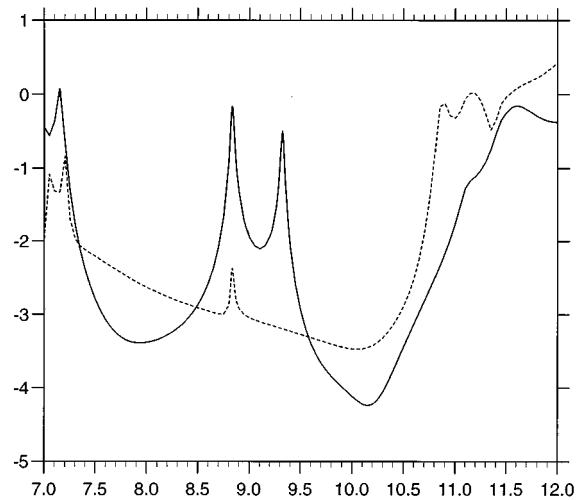


Fig. 13. Decimal logarithm of the transmission  $T$  versus the wavelength for the crystals of Figs. 11 (solid curve) and 12 (dashed curve).

is illuminated in normal incidence, the antisymmetrical mode cannot be excited, and consequently no transmission peak occurs for the wavelength  $\lambda = \text{Re}(\lambda_{p2})$ .

It is worth noting that in Section 4 the location of the defects has been chosen in order to get rid of these symmetry selection rules.

### 6. CONTROLLED EMISSION OF TWO-DIMENSIONAL CRYSTALS

Two-dimensional photonic crystals can be used to obtain light-emitting semiconductor devices with enhanced properties. For instance, by controlling the spontaneous emission, it should be possible to design thresholdless laser diodes.<sup>6,8,16</sup> One of the problems is to enhance emission into modes that escape from the material. This enhancement must occur into a narrow spectral region and into specific directions.

For handling this problem, let us consider the structure of Fig. 16; the source is an infinitely thin wire perpendicu-

lar to the figure plane, and the incident field is given by Eq. (9). This source is located in a microcavity obtained by removing one cylinder, and this cavity lies close to the limits of the crystal, in order to favor extraction of light in the direction normal to the boundary of the crystal. The crystal has the same parameters as those in Sections 3–5. For this structure (without the source), we find a resonant mode for the complex wavelength  $\lambda_p = 9.0575 + i0.015$ . Figures 17 and 18 are obtained when the wire source has a wavelength equal to  $\text{Re}(\lambda_p)$ . The Poynting vector map (Fig. 17) shows that the energy goes outside the crystal through a narrow exit (approximately 1 wavelength wide). Thus diffraction plays a vital role, and the radiation pattern at infinity shows a rather wide range of approximately  $60^\circ$  (Fig. 18). We have also tried some other structures with two or three aligned defects in the crystal, but the results are very similar from the point of view of the angular range of scattered energy.

We now consider the structure of Fig. 19. In the region  $0 < y < 20.8$ , the crystal has the same parameters as those above (the vertical distance between two horizon-

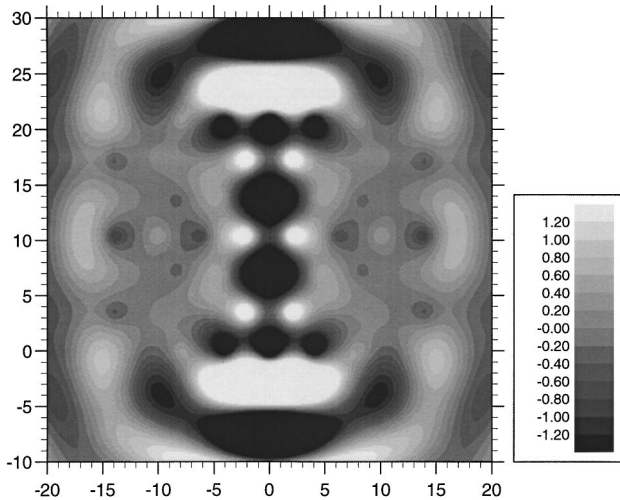


Fig. 14. Real part of the complex field for the mode associated with  $\lambda_{p1} = 8.8335 + i0.0162$  (the crystal is placed as in Fig. 11).

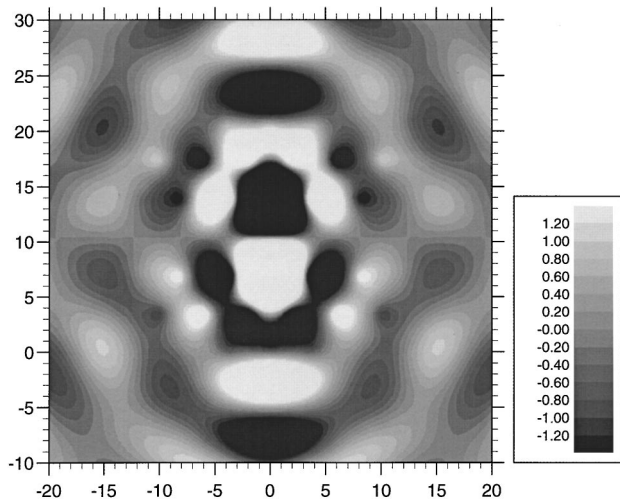


Fig. 15. Real part of the complex field for the mode associated with  $\lambda_{p2} = 9.3210 + i0.0159$  (the crystal is placed as in Fig. 11).

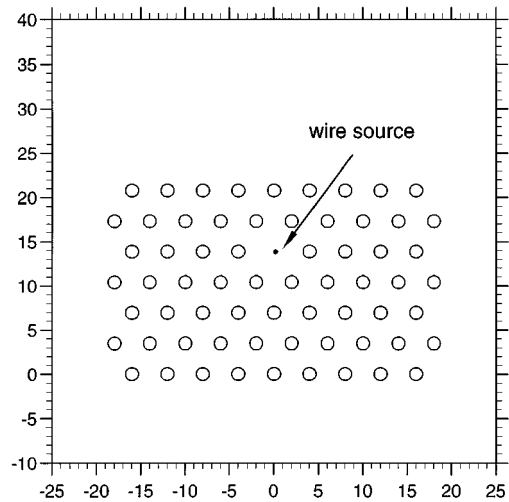


Fig. 16. Wire source located in a cavity close to the limits of the crystal.

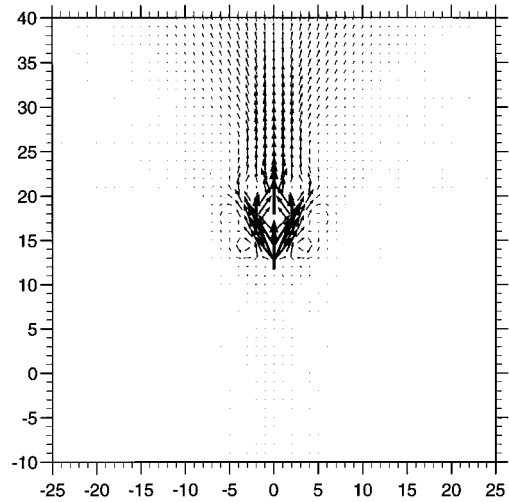


Fig. 17. Poynting vector map for the crystal of Fig. 16. The wavelength of the wire source is  $\lambda = \text{Re}(\lambda_p) = 9.0575$ .

tal grids is  $\sqrt{3}d/2 \approx 3.464$ ). In the region  $20.8 < y < 48.1$ , the crystal has been slightly expanded in the vertical direction in such a way that the vertical distance between two horizontal grids is 3.9. The horizontal spacing  $d = 4$  is unchanged, and the cylinder characteristics are still the same (radius  $\rho = 0.6$ , optical index  $\nu = 2.9$ ). The cavity is obtained here by removing four cylinders.

Let us first give the results obtained by inserting a wire source inside the microcavity of Fig. 19. Figures 20–22 are obtained by locating the thin-wire source at the point with coordinates  $(x = 0, y = 12.7)$ . The wavelength of this source is  $\lambda = 7.934$ . These three figures show, respectively, the total electric-field modulus, the Poynting vector map, and the radiation pattern at infinity. The result is that the energy now flows outside the crystal through a wide aperture (Fig. 21). Consequently, diffraction is much less important than in the preceding example, and the angular range of the radiation pattern is less than  $10^\circ$  wide (Fig. 22). Figure 20 shows that the structure behaves as a resonator. A system of stationary waves is in place between two fictitious interfaces: the

plane between the regularly spaced crystal and the expanded crystal, and the plane between the expanded crystal and vacuum. Looking at Figs. 20 and 21, we can easily see that the width of the outgoing energy path is in fact limited by the dimensions of the structure, which means that the radiation pattern at infinity will become sharper for larger structures.

Let us go now to some more detailed explanations of this phenomenon. One of the key ideas is that the expanded crystal is able to select the direction of propagation.

Figure 23 compares, in normal incidence, the transmissions of a regularly spaced crystal (same characteristics as those in the  $0 < y < 20.8$  region of Fig. 19; i.e., the vertical distance between two horizontal grids is  $\sqrt{3}d/2 \approx 3.464$ ) and of a crystal expanded in the vertical direction (same characteristics as those in the  $20.8 < y < 48.1$  region of Fig. 19; i.e., the vertical distance between

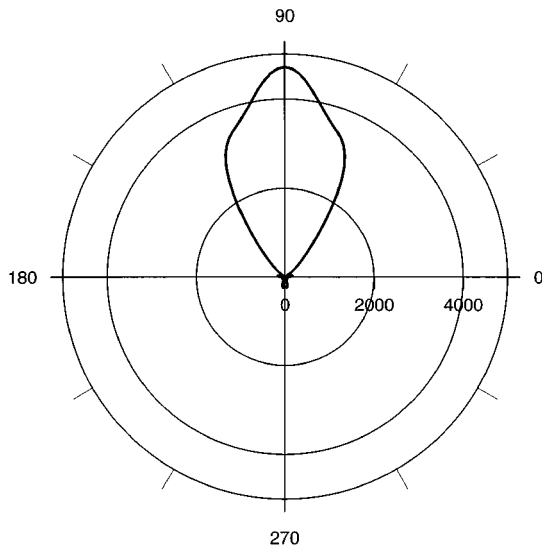


Fig. 18. Radiation pattern at infinity for the crystal of Fig. 16 (polar plot of the intensity at infinity versus the emitting angle). The wavelength of the wire source is  $\lambda = \text{Re}(\lambda_p) = 9.0575$ .

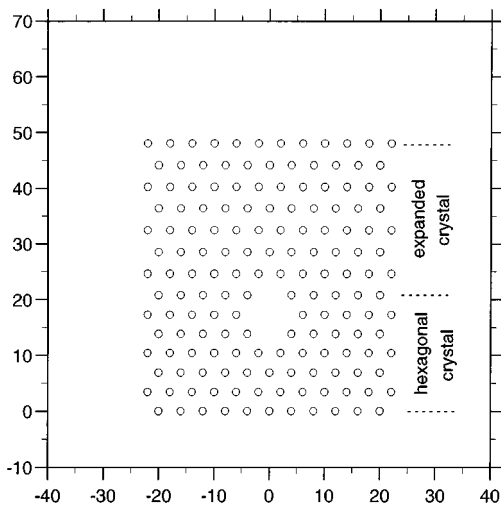


Fig. 19. Superposition of a hexagonal photonic crystal ( $0 < y < 20.8$ ) and of a vertically expanded crystal ( $20.8 < y < 48.1$ ). The cavity is obtained by removing four cylinders.

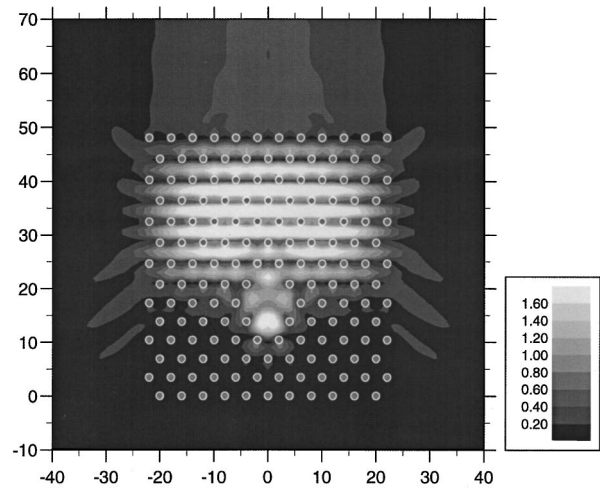


Fig. 20. Total electric-field modulus for the crystal of Fig. 19. The wavelength of the wire source is  $\lambda = 7.934$ .

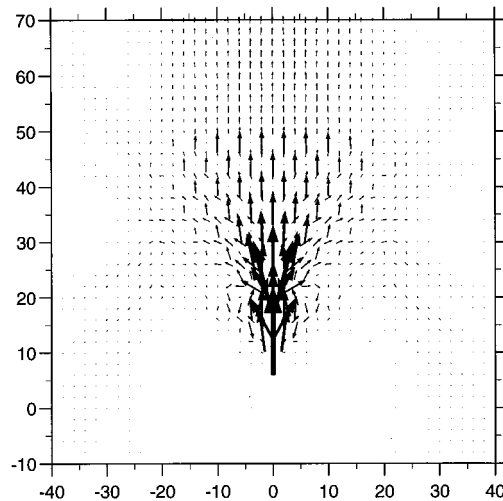


Fig. 21. Poynting vector map for the crystal of Fig. 19. The wavelength of the wire source is  $\lambda = 7.934$ .

tween two horizontal grids is 3.9); both crystals have no defect. Expanding the crystal globally shifts the gap. From this figure it can be concluded that expanding the crystal allows the wavelength  $\lambda = 7.934$  to propagate in the normal (vertical) direction.

Figure 24 compares, for increasing incidences ( $\theta^{\text{inc}} = 0^\circ, 10^\circ, 20^\circ$ ), the transmission of the expanded crystal. Focusing on the particular value  $\lambda = 7.934$ , we can see that the transmission sharply decreases when the incidence is increased.

Broadly speaking, it can be said that the regularly spaced crystal at the bottom of Fig. 19 (in the  $0 < y < 20.8$  region) does not allow propagation of the wavelength  $\lambda = 7.934$  for any direction, whereas the expanded crystal at the top of the same figure (in the  $20.8 < y < 48.1$  region) allows propagation of this wavelength in the vertical direction only.

This phenomenon can be interpreted in a simple way. Let us start from the regular photonic crystal with hexagonal symmetry, and let us expand this crystal in the horizontal and vertical directions with a similarity factor  $\alpha$ . By a straightforward rule of scale, the new gap will be

rigorously deduced from the initial one by multiplying the wavelengths by the same factor  $\alpha$ . One can conjecture that readjusting the radius of the cylinders to the initial value will not strongly change this conclusion. Consequently, expanding the crystal in the vertical direction only should change the band gap in the same way (with multiplying factor  $\alpha$ ) for propagation in this vertical direction, whereas the gap in the horizontal direction of propagation should not be changed drastically.

It is also worth pointing out how the particular wavelength  $\lambda = 7.934$  has been selected. We have seen above that small cavities have resonant wavelengths close to the center of the gap. Such cavities cannot be used here, since we must work at a wavelength close to the boundary

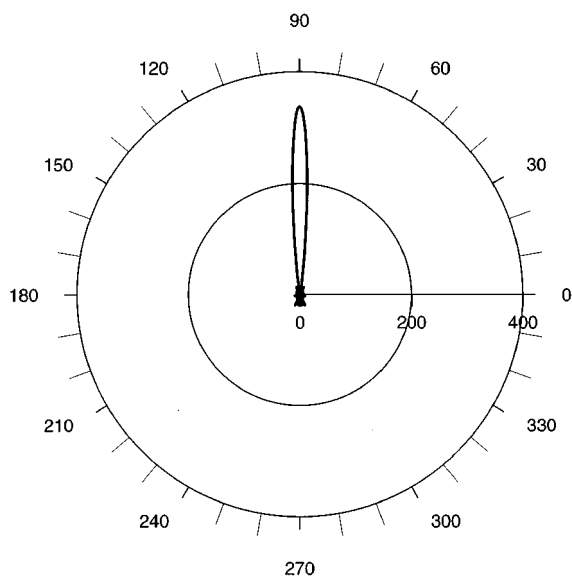


Fig. 22. Radiation pattern at infinity for the crystal of Fig. 19 (polar plot of the intensity at infinity versus the emitting angle). The wavelength of the wire source is  $\lambda = 7.934$ .

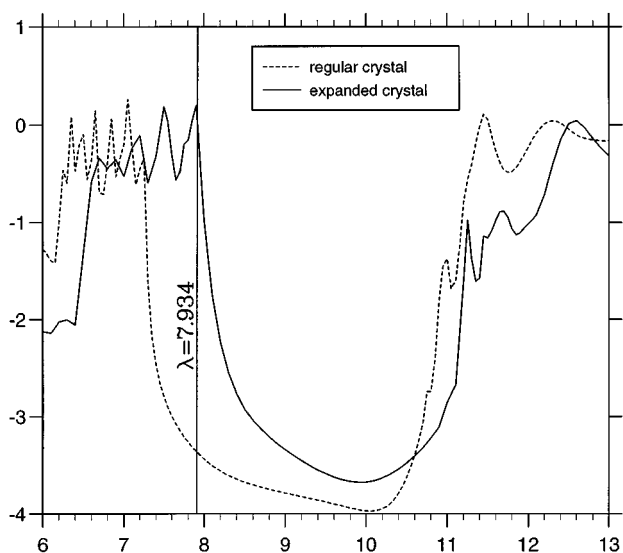


Fig. 23. Decadal logarithm of the transmission  $T$  versus the wavelength for the regularly spaced crystal (dashed curve) and for the vertically expanded crystal (solid curve) for normal incidence. The vertical line corresponds to  $\lambda = 7.934$ .

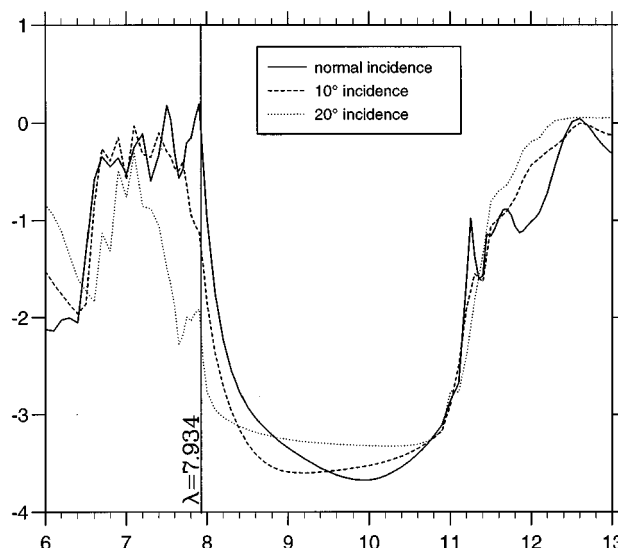


Fig. 24. Decadal logarithm of the transmission  $T$  versus the wavelength for the vertically expanded crystal for different incidences. The vertical line corresponds to  $\lambda = 7.934$ .

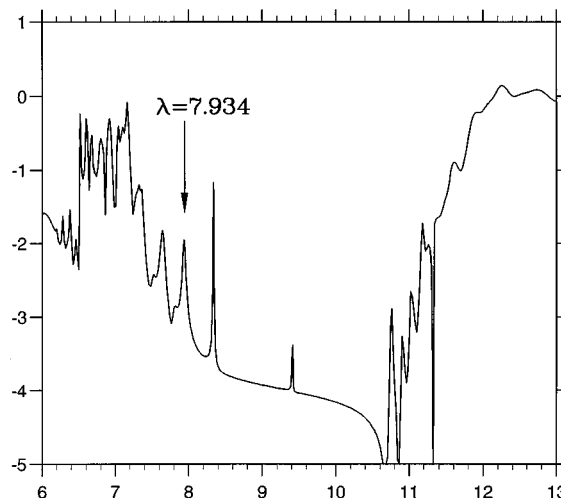


Fig. 25. Decadal logarithm of the transmission  $T$  versus the wavelength for the crystal of Fig. 19 for normal incidence. The marked peak corresponds to the wavelength  $\lambda = 7.934$ .

of the gap (see Figs. 23 and 24). Furthermore, this wavelength must be a resonant wavelength of the cavity. This is the reason why the cavity is obtained here by removing four cylinders. It is much larger than in Sections 3–5 (where only one or two cylinders were removed). The consequence is that several resonant modes appear, and the probability of getting a resonance at the desired wavelength is much greater. Figure 25 gives the transmission for the structure of Fig. 19, illuminated by a plane wave in normal incidence. The peaks give the real part of the complex resonant wavelengths, and the result is that one of these wavelengths is close to the boundary of the gap. This wavelength,  $\lambda = 7.934$ , has been chosen for this study (the complex wavelength for the corresponding mode has been found to be  $\lambda_p = 7.934 + i0.018$ ). The question that arises is the following: Could a structure including a cavity and an expanded crystal be monomode? We are currently trying to answer it.

There is additional interesting information to draw out from the study of the resonant modes. Indeed, the mode field map for  $\lambda_p = 7.934 + i0.018$  shows some regions where the electromagnetic field is very strong. In fact, this map is very similar to that given in Fig. 20. Putting the wire source at a place where the resonant mode is strong gives better coupling between the source and the structure. Consequently, the extraction of energy outside the structure is much greater. This is the reason why the wire source has been located at the point with coordinates  $(x = 0, y = 12.7)$ , where the resonant mode is strong. It has been verified that if the source is placed at the center of the cavity, where the resonant mode amplitude is much less, the radiation pattern at infinity keeps approximately the same shape as that given in Fig. 22, but the maximum value of the intensity (radiated in the  $90^\circ$  direction) falls to approximately 100 (instead of approximately 340 as in Fig. 22).

## 7. CONCLUSION

An efficient numerical tool for the study of microcavities inside a two-dimensional photonic crystal has been presented. The method is able to provide a complete description of all the electromagnetic quantities for crystals of finite size, with short computation time and good precision. All features of this method are used in Section 6, which presents an original way for the control of emission by two-dimensional crystals. Even though the results presented in Section 6 are somewhat academic, the key idea of an expanded crystal could open new directions for people interested in angular-selective devices. Recent experimental studies (as, for instance, those described in Ref. 8) show that the progress of technology makes it possible to design such structures in the optical domain. An experimental verification in the microwave domain of some results obtained in this paper is in progress in our laboratory.

## ACKNOWLEDGMENTS

The work described in this paper has been done under a contract between the Laboratoire d'Optique Electromag-

nétique and the Direction des Recherches Etudes et Techniques (French Ministry of Defence).

## REFERENCES

1. R. D. Meade, A. M. Rappe, K. D. Brommer, J. D. Joannopoulos, and O. L. Alerhand, "Accurate theoretical analysis of photonic band-gap materials," *Phys. Rev. B* **48**, 8434–8437 (1993).
2. J. Joannopoulos, R. Meade, and J. Winn, *Photonic Crystals* (Princeton U. Press, Princeton, N.J., 1995).
3. J. B. Pendry and A. MacKinnon, "Calculation of photon dispersion relations," *Phys. Rev. Lett.* **69**, 2772–2775 (1992).
4. M. Sigalas, C. M. Soukoulis, E. N. Economou, C. T. Chan, and K. M. Ho, "Photonic band gaps and defects in two dimensions: studies of the transmission coefficient," *Phys. Rev. B* **48**, 14121–14126 (1993).
5. P. Villeneuve, S. Fan, and J. D. Joannopoulos, "Microcavities in photonic crystals: mode symmetry, tunability, and coupling efficiency," *Phys. Rev. B* **54**, 7837–7842 (1996).
6. E. Yablonovitch, "Photonic crystals," *J. Mod. Opt.* **41**, 173–194 (1994).
7. D. R. Smith, S. Schultz, S. L. McCall, and P. M. Platzmann, "Defect studies in a two-dimensional periodic photonic lattice," *J. Mod. Opt.* **41**, 395–404 (1994).
8. T. Baba and T. Matsuzaki, "GaInAsP/InP 2-dimensional photonic crystals," in *Microcavities and Photonic Band-gaps: Physics and Applications*, Vol. 324 of NATO Advanced Scientific Institutes Series E, J. Rarity and C. Weisbuch, eds. (Kluwer Academic, Dordrecht, The Netherlands, 1996).
9. D. Maystre, "Electromagnetic study of photonic band gaps," *Pure Appl. Opt.* **3**, 975–993 (1994).
10. D. Felbacq, G. Tayeb, and D. Maystre, "Scattering by a random set of parallel cylinders," *J. Opt. Soc. Am. A* **11**, 2526–2538 (1994).
11. D. Felbacq, D. Maystre, and G. Tayeb, "Localization of light by a set of parallel cylinders," *J. Mod. Opt.* **42**, 473–482 (1995).
12. M. Abramovitz and I. Stegun, *Handbook of Mathematical Functions* (Dover, New York, 1970).
13. N. R. Hill and V. Celli, "Limits of convergence of the Rayleigh method for surface scattering," *Phys. Rev. B* **17**, 2478–2481 (1978).
14. P. M. Van den Berg and J. T. Fokkema, "The Rayleigh hypothesis in the theory of reflection by a grating," *J. Opt. Soc. Am.* **69**, 27–31 (1979).
15. D. Maystre and M. Cadilhac, "Singularities of the continuation of the fields and validity of Rayleigh's hypothesis," *J. Math. Phys.* **26**, 2201–2204 (1985).
16. D. Kleppner, "Inhibited spontaneous emission," *Phys. Rev. Lett.* **47**, 233–236 (1981).